FRINGE 96
Impact of Precise Orbits on SAR Interferometry

Christoph Reigber	GeoForschungsZentrum Potsdam Telegrafenberg A17, D-14473 Potsdam reigber@gfz-potsdam.de
Ye Xia	GeoForschungsZentrum Potsdam Telegrafenberg A17, D-14473 Potsdam xiaye@gfz-potsdam.de
Hermann Kaufmann	GeoForschungsZentrum Potsdam Telegrafenberg A17, D-14473 Potsdam
Franz-Heinrich Massmann	GeoForschungsZentrum Potsdam, GFZ/D-PAF c/o DLR, D-82230 Oberpfaffenhofen fhm@dfd.dlr.de
Ludger Timmen	GeoForschungsZentrum Potsdam Telegrafenberg A17, D-14473 Potsdam timmen@gfz-potsdam.de
Johann Bodechtel	Institute for General and Applied Geology University of Munich Luisenstr. 37, D-803333 München
Michaela Frei	Institute for General and Applied Geology University of Munich Luisenstr. 37, D-803333 München

*

Abstract

For repeat pass SAR interferometry, two precision orbit products from ESA (processed at GFZ/D-PAF, Oberpfaffenhofen) are available: ERS-1/2.ORB.PRC's and ERS-1/2.ORB.PRL's. The conversion of interferogram phases to absolute surface heights require a relative baseline accuracy of 5 cm or even better. In a case study, the preliminary (PRL) and precise (PRC) orbits are used to derive DEMs. The results are compared with existing DTMs. In the test area in Thuringia (Germany), corner reflectors allow an additional accuracy assessment. The impact of orbit uncertainties on D-INSAR deformation analysis is less critical and the PRC's already fulfil the accuracy demands. This is demonstrated by an example from the Dead Sea transform zone in Israel.

Keywords: Precise Orbits, DEM accuracy, corner reflectors

Introduction

Repeat-pass interferometric techniques are employed for generation of topography models (DEMs) and, as a related application, for monitoring temporal surface changes (deformations connected with earthquakes or vulcanism, land sliding, soil erosion). The "state of the art" radar sensors, such as those established on ERS-2 and RADARSAT, acquire SAR image pairs from seperated orbit positions at different epochs. Their accurate knowledge allows a fringe pattern estimation of a reference surface and a conversion from phase differences to surface heights or displacements. Actually, there are uncertainties in the available orbit ephemerides which may distort the imaging geometry significantly. This problem can partly be overcome by using flat areas or sea shores as references. After "flat earth" correction (reduction of ellipsoid fringes), the interferogram fringe pattern must not show any height changes in this parts of the image. The interferogram may be adjusted and a conclusion for the relative orbit positions can be drawn. A more sophisticated approach for baseline assessment is to deploy a radar corner reflector array over the scene, e.g. one line of reflectors in slant range and one in azimuth direction. Unfortunately this can only be done in very few study areas because of the logistical, financial and timing limitations. The most straightforward way to solve the baseline problem is the determination of precision orbits using geodetic satellite tracking techniques like laser ranging and PRARE range and doppler observations. In this paper, the accuracy of the ESA orbit products ERS-1/2.ORB.PRC and ERS-1/2.ORB.PRL is investigated and compared with the SAR interferometry (INSAR) requirements.

ERS orbit accuracy demands

In order to obtain an analytical estimation of the required orbit accuracy for INSAR applications, the mathematical dependency of the interferogram phase from the SAR sensor and the object position have to be understood. In Fig. 1, the across track interferometer geometry is shown with a plain reference surface (for simplification), the sensor positions S_1 and S_2 at altitude H, the object P with elevation h, the baseline components B_X and B_y, the slange ranges R_1 and R_2, and the off-nadir angle (look direction). Because the height h as well as the baseline length B are small compared with H or R, the following equation is valid (Hartl and Xia 1993):

$$\phi = \frac{4\pi}{\lambda}(R_1 - R_2) = \frac{4\pi}{\lambda}\left(B_x\sqrt{1-\frac{H^2}{R_1^2}} - B_y\frac{H}{R_1}\right). \quad (1)$$

By differentiating with respect to B_x, B_y and H, we obtain:

$$\frac{\partial\phi}{\partial B_x} = \frac{4\pi}{\lambda}\sqrt{1-\frac{H^2}{R_1^2}}, \quad \frac{\partial\phi}{\partial B_y} = \frac{-4\pi}{\lambda}\cdot\frac{H}{R_1}, \quad \frac{\partial\phi}{\partial H} = \frac{-4\pi}{\lambda}\left(\frac{B_x H}{\sqrt{1-(H^2/R_1^2)}\cdot R_1^2} + \frac{B_y}{R_1}\right). \quad (2)$$

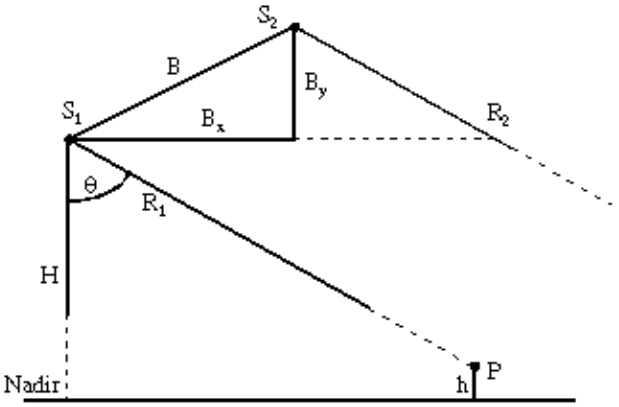

Fig. 1: Imaging geometry of a SAR SLC image pair (S_1, S_2: sensor position at epoch 1 and 2; R_1, R_2: slant ranges to object P; B_x, B_y: baseline components; h: topographic height)

For INSAR the impact of orbit uncertainties on areas with limited extension in ground range are of interest. Therefore, the maximum relative error d = d_{far} - d_{near} has been calculated. The extension of the test areas are assumed to be 5 km (local) and 50 km (regional), and the baseline seperation is considered with 50 m (differential INSAR applications) and 200 m (DEM generation). Approximate parameters of ERS-1 SAR system (= 0.057 m, *H* = 785000 m, $R_{mid\ swath}$ = 853000 m) are introduced in the error equations.

The interferogram phase shows a very low sensitivity to errors in sensor altitude. With dH = 10 m, the effect on topography or displacement is in the order of 1 m or 1 mm. For baseline errors of 0.05 m and 1.00 m, systematic phase errors will be obtained as compiled in Tab. 1. They are converted to surface displacement or topography errors using the equations:

$$d\rho = \frac{\Delta d\Phi}{4\pi}\lambda\,, \quad dh = \frac{\Delta d\Phi}{4\pi}\cdot\frac{R_1\,\lambda\,\tan 23^\circ}{B_x} \qquad (3)$$

To assess the results in Tab. 1, they have to be related to the phase noise which is typically inherent in an interferogram of ERS-1/2 SAR data. The noise is caused by temporal decorrelation (e.g. vegetation, moisture), atmospheric perturbations, geometric baseline decorrelation, as well as data acquisition and processing defects. The validation of radar topography maps yielded errors of 5 to 10 m rms, (e.g. Prati et al. 1993, Small et al. 1993, Schwäbisch 1995, Zebker et al. 1994). This corresponds to a phase uncertainty of about one tenth of the wavelength or 0.6 rad. The phase noise acts mainly locally on a DEM and not systematically over the whole image. The effect of local noise may be a few times larger than the rms values. Therefore, the impact of orbit uncertainties is allowed to be in the order of 0.6 rad or even larger for local displacement analyses.

Tab. 1: Systematic errors for surface heights and displacements due to baseline errors of 0.05 m and 1.00 m. The derived values are related to areas with 5 km (local) or 50 km (regional) spartial extension, and to baseline length of 50 m (for change detection) or 200 m (for topography modelling).

	dB_x=0.05 m	dB_y=0.05 m	dB_x=1.00 m	dB_y=1.00 m
Interferogram Phase Error				
d(5 km) [rad]	0.06	0.02	1.1	0.5
d (50 km) [rad]	0.5	0.2	10.2	4.6
Displacement Error (Slant Range)				
d(5 km) [mm]	0.3	0.1	4.9	2.2
d (50 km) [mm]	2.2	0.9	45.5	20.5
Topography Error, B_x=50 m				
dh(5 km) [m]	2.0	0.7	36.4	16.6
dh(50 km) [m]	16.6	6.6	337.8	152.3
Topography Error, B_x=200 m				
dh(5 km) [m]	0.5	0.2	9.1	4.1
dh(50 km) [m]	4.1	1.7	84.4	38.1

From Tab. 1 the following conclusions can be drawn:

as expected, the across track baseline component B_x is dominant, but the radial component must not be neglected;
to avoid significant systematic errors in topography mapping (e.g. a tilt in ground range direction) a baseline precision of 5 cm has to be striven for;
for the detection of surface uplift or subsidence in areas with local extension, the baseline precision should be better than 1 m; for areas with larger extensions, the baseline should be accurate up to 0.1 m.

At GFZ/D-PAF, the quality of the generated orbit products ERS-1/2.ORB.PRC and ERS-1/2.ORB.PRL is controlled internally by examining the fits of the laser ranges and the altimeter crossovers to the adjusted orbits and by comparing overlapping arc segments (Massmann et al. 1994, Gruber et al. 1996). Results (mean differences) of orbit investigations over a time interval of 6 month are given in Tab. 2.

Tab. 2: Accuracy of ESA orbit products ERS-1/2.ORB.PRC and ERS-1/2.ORB.PRL, derived form internal quality checks (fit of tracking observations to adjusted orbit, comparison of overlapping arc segments)

Orbit Product	radial	across	along
.PRC	7 cm	33 cm	31 cm
.PRL	8 cm	35 cm	35 cm

As shown in Tab. 2 the accuracy of .PRC and .PRL products is very similar. The demanded accuracy of 5 cm for DEM generation is not achieved, which makes a baseline estimation during the interferometric SAR processing still necessary. Such an estimation can serve as an external test of the orbit quality and will help to find out, whether there are advantages of .PRC orbits compared to .PRL orbits.

Application of ESA ERS-1/2 orbit products

In this section we provide two INSAR products generated with the ESA orbit products (humid climate in Germany, arid climate along the Dead Sea Rift). It is demonstrated how the orbit is used to generate the fringe pattern of a reference flat surface and what the orbit accuracy is.

In the first example a digital elevation model (DEM) is generated for the test area Ronneburg in Thuringia/Germany (50.8° N and 12.2° E). The single look image data pair was acquired during a tandem operation on the 8th of Feb. 1996 by ERS-1 and on the 9th. of Feb. 1996 by ERS-2. Fig. 2 shows the intensity of the SAR image over an area of 30 km in azimuth and 40 km in ground range. As reference the ellipsoid surface of WGS84 is applied. The following equation models the fringe pattern of the ellipsoid surface for a slant range line in the interferogram:

$$\varphi_{(i)} = 2\pi(c_0 + \frac{1}{2}c_1 i + \frac{1}{3}c_2 i^2)i + \varphi_0 \tag{4}$$

Here, is the phase of the pixel *i* (*i* is normalized by image pixel number *N-1* from *0* to *1*), $_0$ is the initial phase of the considered line, c_0, c_1, and c_2 are the polynomial coefficients. The instantaneous fringe frequency derived from Eq. 4 is:

$$f_{(i)} = c_0 + c_1 i + c_2 i^2 \tag{5}$$

In order to calculate the polynomial coefficients c_0, c_1, and c_2 the following linear equation system has to be solved:

$$\begin{bmatrix} f_0 \\ f_{1/2} \\ f_1 \end{bmatrix} = \begin{bmatrix} 1 & 0 & 0 \\ 1 & 0.5 & 0.25 \\ 1 & 1 & 1 \end{bmatrix} \begin{bmatrix} c_0 \\ c_1 \\ c_2 \end{bmatrix} \tag{6}$$

Here f_0, $f_{1/2}$ and f_1 are the instantaneous fringe frequencies by *i=0*, *1/2* and *1*, respectively.

The mathematical representation of the orbit (position and velocity) for the primary and the secondary satellite is identical, but with different coefficients:

$$\begin{cases} x_{(t)} = \sum_{n=0}^{4} a_n t^n \\ y_{(t)} = \sum_{n=0}^{4} b_n t^n \\ z_{(t)} = \sum_{n=0}^{4} c_n t^n \end{cases} \tag{7}$$

The coefficients are derived from the precision orbit ephemerides as determined by GFZ /D-PAF in accordance with the image acquisition time. By means of the orbital state (position vector $\vec{S}$ and velocity vector $\vec{V}_s$) and using equations from Curlander (1982), the pixel coordinate $P_{(Xp, Yp, Zp)}$ for *i=0*, *1/2*, and *1* can be determined for each slant range line:

(8)

$$\begin{cases} \dfrac{\left(x_p^2+y_p^2\right)}{R_A^2}+\dfrac{z_p^2}{R_p^2}=1 & \text{ellipsoid equation} \\ \dfrac{2}{\lambda R_s}(\vec{V}_s-\vec{V}_p)\cdot(\vec{S}-\vec{P})=f_d & \text{doppler equation} \\ \sqrt{(\vec{S}-\vec{P})\cdot(\vec{S}-\vec{P})}=R_s & \text{distance equation} \end{cases}$$

The position of the secondary satellite according to object *P* is obtained by solving the following equation:

$$\left(x_{(t)}-x_p\right)\frac{dx_{(t)}}{dt}+\left(y_{(t)}-y_p\right)\frac{dy_{(t)}}{dt}+\left(z_{(t)}-z_p\right)\frac{dz_{(t)}}{dt}=0. \quad (9)$$

As soon as the satellite positions and pixel position for *i=0*, *1/2*, and *1* are known, the instantaneous fringe frequency is obtained from equation

$$f_{(i)}=\frac{\Phi_{i+1/N}-\Phi_i}{2\pi}N. \quad (10)$$

Removing the fringe pattern of the reference surface, the residual phase (or so-called relative phase) remains, which is shown in Fig. 3. After phase unwrapping and conversion from phase to height (Fig. 4), a comparison between the INSAR elevation model using .PRC orbits and the DEM derived from aerial photogrammetry (Fig. 5) can be carried out. Fig. 6 shows a systematic slope error of 65 m in across direction from near range to far range (40 km). In this case (baseline=142 m) the systematic slope error of 65 m is equivalent to a fringe frequency error of 0.89 or a baseline error of 62 cm. Fig. 7 compares the corrected height model derived from INSAR with the DGM. In the test area of 30 km * 40 km the standard deviation is 8.5 m (or in phase 40°) and the mean difference is -0.06 m. The maximum differences occur in the area of the open-cast mining where large mass movements (depositing of slagheap material in the open pit) are taking place since several years.

To compare the accuracy of the ESA orbit products ERS-1/2.ORB.PRC and ERS-1/2.ORB.PRL, the Ronneburg data set is evaluated with each of them. In Tab. 3, the fringe frequencies are calculated for the first slant range line as an example, the baseline is estimated in the middle of this line. The improvement of fringe frequency and baseline estimation by using of the .PRC orbit instead of the .PRL orbit is only 0.05 and 4 cm, respectively. This result confirms the assessment from the internal quality checks of the GFZ/D-PAF [Tab. 2].

Tab. 3: Comparison of the fringe frequencies and the corresponding baseline after applying the ESA orbit products ERS-1/2.ORB.PRC and ERS-1/2.ORB.PRL: *the improvement for fringe frequency and baseline is 0.05 and 4 cm, respectively*

	fringe f_0	fringe $f_{1/2}$	fringe f_1	baseline (m)
derived from PRC	223.09	204.06	188.03	141.92
derived from PRL	223.04	204.01	188.98	141.88

During the SAR data acquisition in Feb. 1996, 5 passive corner reflectors (CRs) were available in the test area, all positioned by GPS (5 mm accuracy). Tab. 4 compares the heights derived from INSAR and GPS for all CRs.

Tab. 4: Comparison of CR heights derived from INSAR and from GPS: *CR 2 was chosen as reference point, as level ellipsoid the parameters of WGS84 are used .*

Corner No.	Height (GPS)	Height (INSAR)	Height Difference
1	306.25m	305.42m	0.83m
2	295.50m	295.50m	0.00m
3	335.75m	333.45m	2.30m
4	328.32m	324.96m	3.36m
9	379.67m	369.40m	10.27m

The CR 2 was chosen as the reference point. The maximum difference occurs for CR 9 and amounts to 10.27 m. A big metaled light, fixed to a wooden post in about 5 m altitude, and not removed at that time was just in the direction from CR 9 to the satellite. This would explain the large discrepancy. Considering the first 4 CRs, the result is very good. The differences correspond to a radar wave resolution of 1 mm.

In order to check the impact of the ERS PRC orbits on geocoding of INSAR images, a positioning procedure for all CRs were accomplished by use of the Eq. (7), (8) and the CR heights as derived from GPS. The result is shown in Tab. 5, the global geocentric coordinate system of ITRF is used and the all differences were transformed into a local astronomical coordinate system. The positioning accuracy for all CRs is in the order of several meters. It must be noted that the resolution of the sampling in slant range is 7.9 m, in azimuth direction about 4 m, or the pixel spacing of ERS-1 and ERS-2 is 20 m*4 m related to the Earth's surface.

Tab. 5: Comparison of the positioning results: *the global coordinate system of ITRF is used and all differences are transformed into a local astronomical coordinate system*

Corner	X (m)	x (m)	Y (m)	y (m)	Z (m)	z (m)

Number	GPS	INSAR		GPS	INSAR		GPS	INSAR	
1	3939304.5	3939312.5	6.1	855789.4	855793.3	-0.5	4926507.9	4926509.5	6.8
2	3939234.6	3939243.2	2.9	856216.2	856213.7	-6.0	4926476.4	4926478.5	6.8
3	3940137.9	3940145.2	3.1	854230.7	854234.1	0.1	4926152.6	4926155.0	7.0
4	3940583.2	3940590.5	4.0	855904.6	855905.3	-2.6	4925500.6	4925503.5	6.9
9	3945132.2	3945147.0	-1.3	851565.0	851564.5	-6.3	4922695.9	4922693.0	7.0

The second example concerns the detection of subtle surface changes along the Dead Sea Rift, the natural border between Israel and Jordan. The zone is well known as an active plate boundary, marked by e.g. 32 earthquakes with magnitude > Ms. 4.5 in 1993. Using the differential SAR interferometry technique the area has been investigated because an earthquake occured on November 22, 1995, near the transform zone in the Gulf of Elat/Aqaba to the south. In 1995 three single look complex image sets were acquired: on August 16 (21373/585) and on November 29 (22878/585) by ERS-1, and on September 21 (2201/585) by ERS-2, respectively. Fig. 8 shows the intensity image of the test area (29.24° N / 34.55 ° E, 40 km*40 km). First we have calculated two interferograms from the three data sets. The one pair (21373/585 and 2201/585) with a baseline of 308 m spans 35 days, the other one (21373/585 and 22878/585) with a baseline of 76 m spans 105 days. In each case the fringe pattern of the reference surface was removed using the precise orbits. After phase unwrapping the first interferogram was normalized with the baseline rate, and was subtracted from the corresponding second interferogram. The result focussing on the transform zone is shown in Fig. 9, where no distinct changes due to coseismic displacements can be observed. This is mainly due to the fact that the epicenter of the earthquake is located about 100 km to the south in the Gulf of Aqaba/Elat. Nevertheless, observable subtle changes in the data are various. There is an increasing level (blue) of a surface mud-dump to the north caused by mining activities at the Timma Complex to the southwest. Decreasing values (red) are displayed by partly harvested vegetation areas (south) covering the northern rim of the Gulf, and by pediments and alluvial fans at the western part of the rift. Most of the phenomena can also be attributed to heavy rains within the given recording frame. Assuming that the accuracy of the baseline estimation by use of the precise orbits is in the range of 1 m, and that the standard deviation of the relative phase is not more than 40°, the accuracy of the detected mass movements is approximate 0.3 cm.

Conclusions

The accuracy requirement of the satellite orbits for SAR interferometry is discussed in this paper. To avoid significant systematic errors, a baseline accuracy of 5 cm for DGM generation and of better than 1 m for subtle change or mass movement detection has to be striven for. The comparison of an elevation model derived from INSAR by use of ESA precise orbits with the existing DEM demonstrates that ESA precise orbits provides a baseline accuracy of better than one meter. This satisfies the D-INSAR needs in most cases. A positioning example of CRs shows that an accuracy of 1 resolution cell may be achievable. For the goal of DEM generation, the employment of CRs and their GPS survey is still essential.

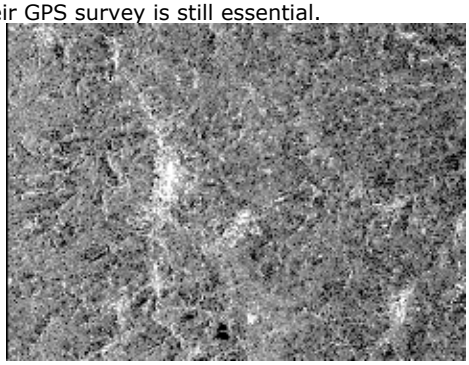

Fig. 2 Intensity image of the test area Ronneburg

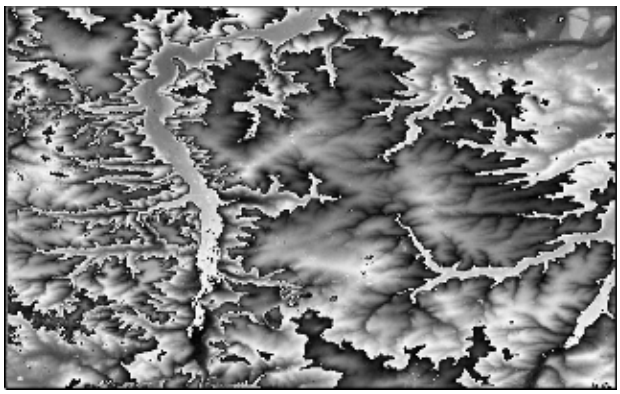

Fig. 3 Relative phase image by use of .PRC orbits

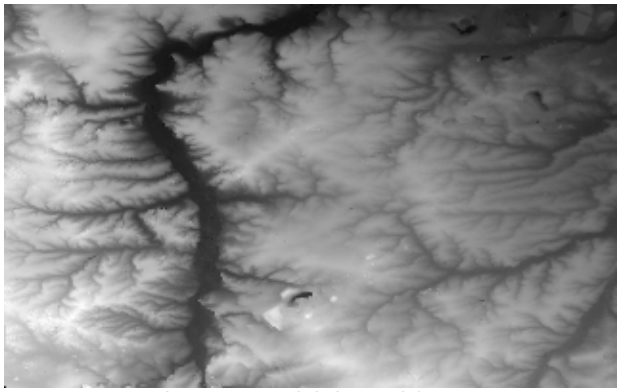

Fig 4. Elevation model derived from INSAR

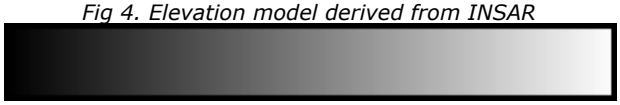

105 m 393 m

Fig. 5 Existing DEM derived from photogrammetry

148 m 386 m

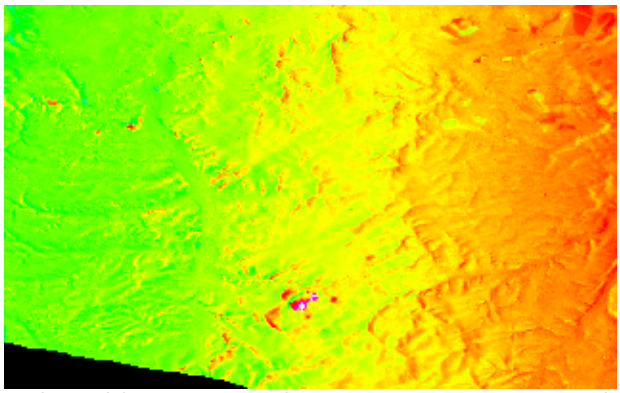

Fig. 6 Height difference between DEM derived from INSAR and existing DEM: a systematic slope error of 65 m in across direction (40 km) corresponds to a fringe frequency error of 0.89 or to a baseline error of 62 cm.

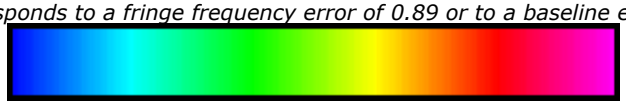

-45 m 40 m

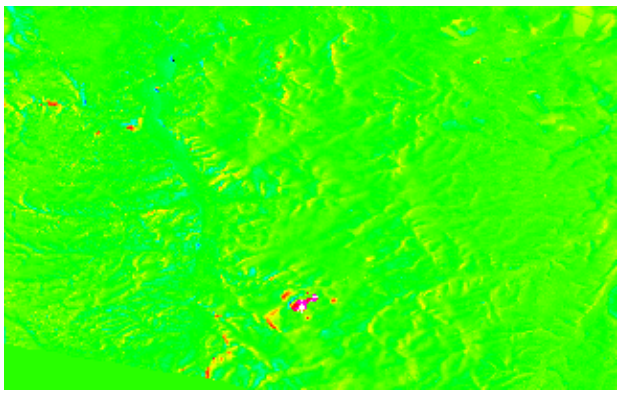

Fig. 7 Height difference between corrected DEM derived from INSAR and existing DEM: *mean=-0.06 m, standard deviation=8.5 m, the maximum differences occur in the area of the open-cast mining.*

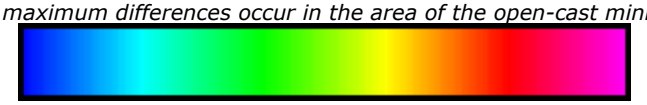

-112 m 106 m

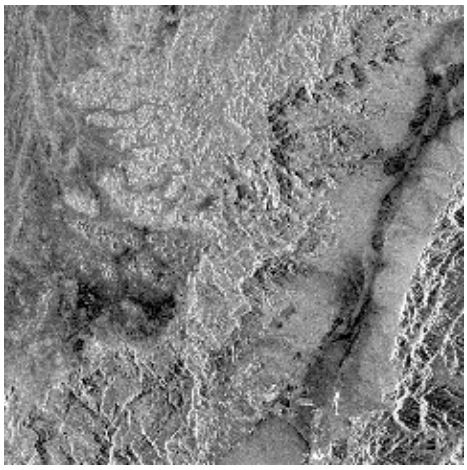

Fig. 8 Intensity image of an area north of the Gulf of Elat/Aqaba (Israel/Jordan): the scene site is *29.24° N / 34.55° E*, the area is 40 km * 40 km.

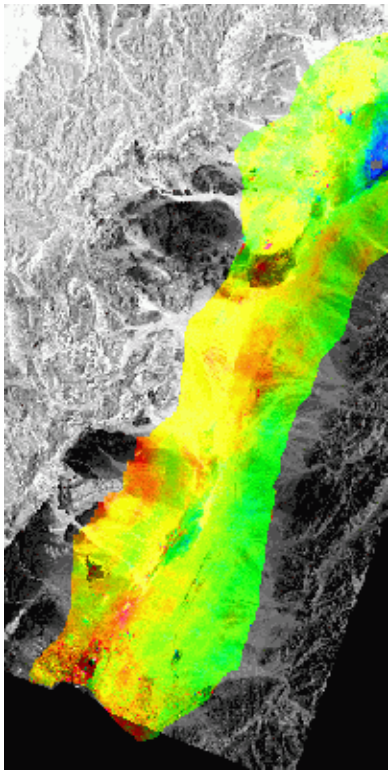

Fig. 9 Result of D-INSAR for the Dead Sea Rift area in the transform zone near Elat/Aqaba: *the data sets were acquired at 16.08.95, 21.09.95 and 29.11.95. IHS-color merge of optical (Landsat TM band 4) and differential INSAR result (I=TM, H,S =D-INSAR).*

1.4 cm 0 -1.4 cm

References

Curlander, J. C. 1982:
Location of Spaceborne SAR Imagery*, IEEE transaction on Geoscience and Remote Sensing,* Vol. 20, N0. 3, pp. 359-364

Gruber, Th., Massmann, F.-H., Reigber, Ch., 1996:
The German PAF for ERS, ERS D-PAF altimeter and global products manual, ERS-D-GPM-31200.

Hartl, Ph., Xia Ye 1993:
Datenverarbeitung bei der SAR-Interferometrie*, Zeitschrift für Photogrammetrie und Fernerkundung,* 6/93, pp. 214-222

Massmann, F.-H., Reigber, Ch., König, R., Ralmondo J. C., Rajasenan, C., 1994:
ERS-1 orbit information provided by D-PAF. *Proceedings Second ERS-1 Symposium - Space at the Service of our Environment, Hamburg, Germany, 11-14 October 1993, ESA SP-361, pp. 765-770.*

Prati, C., Rocca, F., Monti Guarnieri, A., 1993:
SAR *interferometry* experiments with ERS-1. *Proceedings First ERS-1 Symposium - Space at the Service of our Environment, Cannes, France, 4-8 November 1992, ESA SP-359, pp. 211-218.*

Schwäbisch, M. ,1995:
Die SAR-Interferometrie zur Erzeugung digitaler Geländemodelle. DLR-Forschungsbericht 95-25, Deutsche Forschungsanstalt für Luft und Raumfahrt e.V. (German Aerospace Research Establishment), Köln, 125 pages.

Small, D., Werner, C., Nüesch, D., 1993:
Baseline modelling for ERS-1 SAR Interferometry. Proceedings of IGARSS´93, Tokyo, pp. 1204-1206.

Zebker, H., Werner, C., Rosen, P., Hensley, S., 1994:
Accuracy of topographic maps derived from ERS-1 interferometric radar. IEEE Transactions on Geoscience and Remote Sensing, Vol. 32, No. 4, pp. 823-836.